photonics

MDPI

Article

Impact Point Localization Method Using Dual-Rectangular-Ring Linear Optical Microphone Array Based on Time-Equivalent Model

Chenxi Duan, Jinping Ni *, Hui Tian, Yubo Wang and Jing Li

School of Optoelectronic Engineering, Xi'an Technology University, Xi'an 710021, China; cherokeedcx@126.com (C.D.); tianhui@xatu.edu.cn (H.T.); wyb05112025@163.com (Y.W.); zyqinglj@163.com (J.L.)
* Correspondence: nijp6504@263.net

Abstract

In terminal flight trajectory, significant dispersion poses a challenge for accurate localization, as the velocity vector of a supersonic flying object increasingly deviates from the normal vector of the measurement plane under gravitational and aerodynamic effects. Therefore, in this study, an impact point localization method, utilizing a dual-rectangular-ring linear optical microphone array based on apparent shock-wave velocity, was developed. A shock-wave measurement array was developed using a dual rectangular ring composed of linear optical microphone arrays. A time-equivalent model, derived from shock-wave propagation, was introduced to analyze the apparent velocity of the shock-wave within the measurement plane. The time difference in the shock-wave arrivals at the dual rectangular ring, combined with the distances between the inner and outer rectangular rings, was used to calculate the non-uniform apparent shock-wave velocity, thereby enabling the localization of supersonic flying objects. The method's constraints were examined, and its measurement errors were evaluated. The simulation and experimental results showed that the error was less than 0.5 mm. The proposed novel and cost-effective method for impact point localization aids in the effective dispersion assessment of flying objects.

Keywords: impact point localization; supersonic flying object; shock-wave; linear optical microphone array; dual-rectangular-ring

1. Introduction

Evaluating the dispersion of flying objects (FOs) [1,2] requires measuring the position of their impact points (IPs) as they pass through the measurement plane. FO velocity forms a small inclination angle ($\leq 5°$) with the normal vector of the measurement plane, or is parallel to it, and this is defined as the normal incidence model [3]. In the case of a supersonic FOs, an axisymmetric body of revolution passes through the measurement plane; the FO's velocity and normal vector form an inclination angle >5° due to the effects of gravity and air resistance, and this is defined as the oblique incidence model [4]. Additionally, jump angles [5] generated during the launching process may further exacerbate the oblique incidence. FO localization is also essential for evaluating the protection performance of armor materials [6,7], the impact resistance of aerospace skin structures, and for localizing impact sites caused by space debris [8,9]. Current IP positioning methods are primarily optical and acoustic in nature, and exhibit several limitations.

Optical methods include three scenarios. The first one is the multi-light-screen array [10,11], where the core detection element, the light screen (LS), is typically of two

Check for updates

Received: 18 December 2025
Revised: 17 January 2026
Accepted: 22 January 2026
Published: 23 January 2026

types. The A-type is the lens LS sensor [12,13], with subtypes depending on background light conditions. The B-type uses an opposing configuration of array light sources at the transmitter and photoelectric detectors at the receiver [14]. Generally, the multi-light-screen array models the LS as a mathematical plane with no thickness. However, some studies [15] have incorporated the screen's thickness into IP measurements. The second scenario, the laser-based LS [16,17], has also been employed for the detection and localization of FOs. The third scenario is the dual charge-coupled device (CCD) intersection measurement system [18,19], which uses two linear or area CCD sensors intersecting at a specific angle within the measurement plane to perform coordinate measurements. In optical methods, the non-uniform sensitivity of all LS scenarios may significantly reduce the amplitude of the FO signal at certain positions [20,21]. In more severe cases, the signal may be buried in noise, leading to increased errors or the failure of time-difference algorithms. These issues are further amplified in large measurement planes ($\geq$10 m $\times$ 10 m), potentially causing significant errors or incorrect results.

In acoustic IP measurement, piezoelectric sensors [22] are commonly used to detect the shock-wave (SW) from the supersonic axisymmetric body-of-revolution object. Due to the wide propagation range of SWs, the measurement plane in acoustic methods typically covers a large area. The acoustic approach primarily uses the time difference of arrival (TDOA) [23] to determine the location of the sound source. It establishes a mathematical model for IP localization based on the time difference in SW arrivals at different sensors. Acoustic sensors are arranged in various configurations, such as double triangular [24], T-shaped [25], or tetrahedral arrays [26]. However, accurate IP localization is typically limited to cases where the FO's velocity vector is perpendicular to the measurement plane. Lin [4] proposed a location model for FOs with oblique incidence using a double triangular array, while Dong [27] introduced an open seven-element array for the same purpose. However, their methods are limited to IP measurements at small angles of incidence ($\leq$5°).

Optical microphones [28] are categorized into several types, such as fiber-optic acoustic pressure sensors [29,30], laser interferometry-based microphones [31], optical MEMS microphones [32], and thermally stable optical microphones [33]. These sensors generally employ various optical measurement principles to replace traditional piezoelectric acoustic sensors, while also functioning as point-type sensors for SW measurements. However, point-type sensors can only capture the arrival time of an SW at a single spatial point. When deployed to form a coplanar feature sensor array, they impose additional constraints. Moreover, as the FO moves farther away from the point sensor, the amplitude of the acquired SW signal decreases. This reduction in signal strength can introduce errors in identifying characteristic timestamps during time-difference calculations, ultimately leading to increased localization errors.

With the increasing application of deep learning in target localization [34], data-driven methods have demonstrated considerable advantages in recognizing complex patterns, such as those in images and acoustic signals. However, in the specific physical context of localizing a supersonic FO, deep learning-based localization methods face several fundamental challenges: (1) their "black-box" nature results in a lack of interpretability, making it difficult to trace localization errors back to specific physical causes [35]; (2) they require vast amounts of labeled training data, which are extremely difficult to acquire for FO scenarios due to the high cost of experiments and the scarcity of controlled samples [22,36]; and (3) their generalization capability is limited for conditions outside the training data distribution (e.g., changes in array size or shock-wave parameters), and they often demand substantial computational resources, failing to meet the stringent requirements of edge computing and real-time closed-loop control [37].

In this paper, we present a localization method for supersonic FOs using a dual-rectangular-ring linear optical microphone array (DRRLOMA) to measure the arrival time of the SW. Unlike traditional point-array acoustic sensors that detect SWs at discrete points, each linear optical microphone (LOM) performs continuous sensing along its laser path, enabling detection closer to the FO trajectory and acquiring higher-intensity SW signals. Additionally, the proposed method is centered on a well-defined physical model, requires no training data, and achieves localization directly through analytical computation. This approach not only ensures process transparency and result traceability but also offers the flexibility to adapt to FO measurement scenarios of varying scales. It thereby provides a viable technical pathway for the reliable and precise localization of supersonic FOs. Additionally, the measurement method proposed in this paper is immune to interference from the muzzle flash [38] and the tail flame of tracer rounds [39].

The main contributions and highlights of this work are as follows:

1. To achieve large-area SW detection, a DRRLOMA, composed of linear optical microphone arrays, was developed. By leveraging the broad propagation characteristics of SWs [40] and the collimation properties of lasers, an array comprising eight LOMs was designed and arranged in both inner and outer rectangular ring configurations.
2. A time-equivalent model, minimum-time SW path, converts spatial SW propagation into the apparent shock-wave velocity (ASWV) propagation time within the measurement plane by decomposing the path into the FO's travel time to the interception point (IP) and the ASWV propagation from the IP to a given LOM. Due to the deterministic FO trajectory, the temporal reference shifts to the instant the object reaches the measurement plane, enabling this transformation.
3. To determine the IP, in this study, we propose a method for localizing FOs based on a DRRLOMA. By introducing a shock-wave propagation time-equivalent model, the non-uniform propagation characteristics of ASWV within the measurement plane—following the oblique incidence model of the FO—are calculated, enabling high-precision determination of the IP.

2. DRRLOMA Setup and IP Localization Method

2.1. LOM Setup

As shown in Figure 1, the structure of the LOM consists of a point laser source located at the transmitter and a photodetector positioned at the receiver. These two components are separated by a distance denoted as l_{om}. The transmitter consists of four components: a point laser, aperture stop, laser holder, and laser driver circuit. The receiver comprises three components: a photodetector, a photoelectric conversion circuit, and an amplification circuit. For convenience in subsequent descriptions, the transmitter and receiver of the LOM are topologized.

Figure 2a shows the principle of the LOM. When the SW arrives at the laser path of the LOM, it alters the refractive index distribution along the propagation path [41], causing the laser beam to deflect. The corresponding displacement of the laser spot on the photosensitive surface of the receiver's photodetector induced by the SW is illustrated in Figure 2b. As a result, the irradiance on the photosensitive surface S_{OAS} of the receiver's photodetector decreases by ΔE_{OAS}. The corresponding change in radiant flux, denoted as $\Delta\phi$, can be expressed as

$$\Delta\phi = \Delta E_{\mathrm{OAS}} \cdot S_{\mathrm{OAS}} \tag{1}$$

In the amplification circuit of the LOM in the receiver, the output voltage signal $V_{\Delta\phi}$ is proportional to $\Delta\phi$ and is denoted by

$$V_{\Delta\phi} = \varepsilon\gamma_0 R\Delta\phi > U_{\Delta\phi} \quad \rightarrow \quad V_{\Delta\phi} \propto k_{OAS}\Delta\phi > U_{\Delta\phi} \tag{2}$$

where k_{OAS} corresponds to the rate of change between $V_{\Delta\phi}$ and $\Delta\phi$. $U_{\Delta\phi}$ is the threshold voltage of the LOM. The signal waveform corresponding to $\Delta\phi$, denoted as $V_{\Delta\phi}$, is shown in Figure 2c. ε indicates the sensitivity of the LOM, γ_0 represents the circuit amplification, and R is the current–voltage conversion resistor.

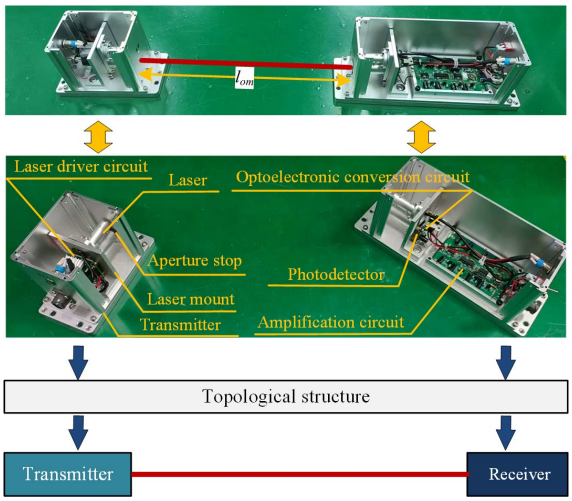

Figure 1. Structure of LOM.

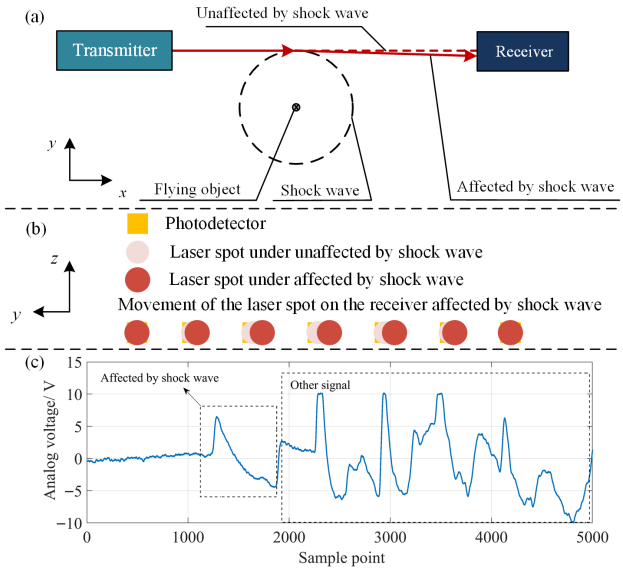

Figure 2. (**a**) Principle of the LOM; (**b**) displacement of the laser spot affected by the SW; (**c**) signal of $\Delta\phi$.

2.2. DRRLOMA Setup

Figure 3a illustrates the LOM configuration in a rectangular ring. The transmitter and receiver are arranged orthogonally, such that the A-transmitter and the B-receiver together form a single LOM unit, the B-transmitter and the C-receiver together form a single LOM unit, the C-transmitter and the D-receiver together form a single LOM unit, and the D-transmitter and the A-receiver together form a single LOM unit. Figure 3b shows the structure of the dual rectangular ring. Four LOM units form an inner rectangular ring with a side length of l_{om}. An additional four LOM units form an outer rectangular ring with a side length of $l_{om} + 2S_{om}$. The spacing between the inner and outer rectangular rings is S_{om}, and both rings lie in the same plane. The rectangular area enclosed by the inner rectangular ring serves as the effective region of the measurement plane. The dual-rectangular-ring

SW measurement array, DRRLOMA, consists of coplanar inner and outer rectangular rings composed of linear optical microphone arrays. The SW propagates through the air and the SW-induced acoustic signal is captured through changes in the laser path within the DRRLOMA. The SW reaches the laser path of the LOM, where its arrival is characterized by an optical microphone detection mechanism. Therefore, the localization of supersonic FOs is based on detecting the SW arrival times at the DRRLOMA.

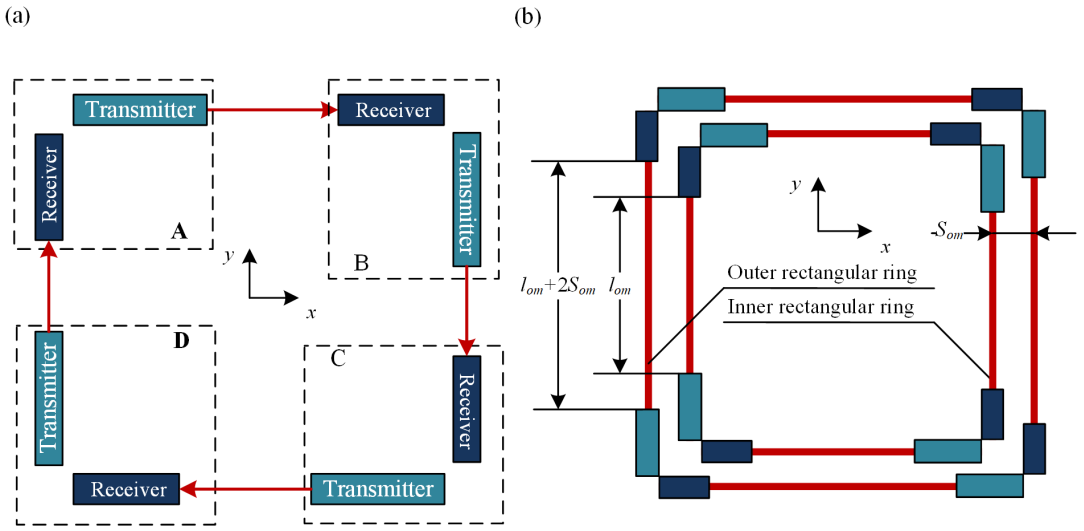

Figure 3. (**a**) Schematic of a rectangular ring; (**b**) schematic of the dual rectangular ring.

2.3. Time-Equivalent Model of Shock-Waves

A two-dimensional equivalent model [27] can be defined as follows: within a two-dimensional measurement plane, the minimum propagation time for a shock-wave to reach a sensor corresponds to the shortest acoustic path, which is oriented perpendicular to the shock wavefront. This process can be decomposed into two distinct components: the motion of the FO along its trajectory and the propagation of the ASWV vector within the measurement plane.

Therefore, a three-dimensional equivalent model can be defined as follows: within the three-dimensional measurement plane, the shortest shock-wave propagation time—from the initiation point of the shortest path on the FO's trajectory to a given LOM in the measurement plane—is defined as an equivalent ASWV propagation time from the IP to that LOM. The core assumption of the model is that the minimum-time shock-wave path in space can be decomposed into two components: (i) the travel time of the FO from the trajectory point corresponding to the initiation of the shortest shock-wave path to the IP on the measurement plane, and (ii) the ASWV propagation time from the IP to the given LOM within the measurement plane. Since the FO follows a continuous and deterministic trajectory, the temporal reference of shock-wave propagation can be shifted to the instant when the object reaches the measurement plane. As a result, the shock-wave propagation to each LOM can be fully characterized by the ASWV within the measurement plane.

Assume that the FO velocity vector is v, the azimuth is γ (positive clockwise and negative counterclockwise), the pitch angle is θ (positive upward and negative downward), the half-shock angle of FOs is α, and the SW propagation velocity is the ambient sound speed c_0. The LOMs on the left and bottom sides of the inner rectangular ring serve as the x-axis and y-axis, respectively. The distance between the inner and outer rectangular ring is S_{om}. Their intersection is defined as the origin o of the o-xyz, and the measurement plane is the xoy plane of the o-xyz. In the xoy plane, a-, b-, c-, and d-directions represent the negative x-axis, negative y-axis, positive x-axis, and positive y-axis, respectively. The

positions labeled 1 and 2 correspond to the inner and outer rectangular ring, respectively. The SW arrival times at the LOMs a_1, a_2, b_1, b_2, c_1, c_2, d_1, and d_2 are denoted as t_{a1}, t_{a2}, t_{b1}, t_{b2}, t_{c1}, t_{c2}, t_{d1}, and t_{d2}, respectively. The schematic of the SW propagation process is shown in Figure 4. D is a point on the trajectory, and the trajectory DP intersects the measurement plane at the IP P (x_P, y_P, z_P), where $z_P = 0$. The distance of DP is l. The FO moves from D to N_{a1} along its trajectory at velocity v. The conical wavefront of the SW becomes tangent to the laser path of the a_1 at U_{a1}. The propagation distance of the SW from the trajectory to a_1 is minimized at N_{a1}, and the minimized distance is $N_{a1}U_{a1}$.

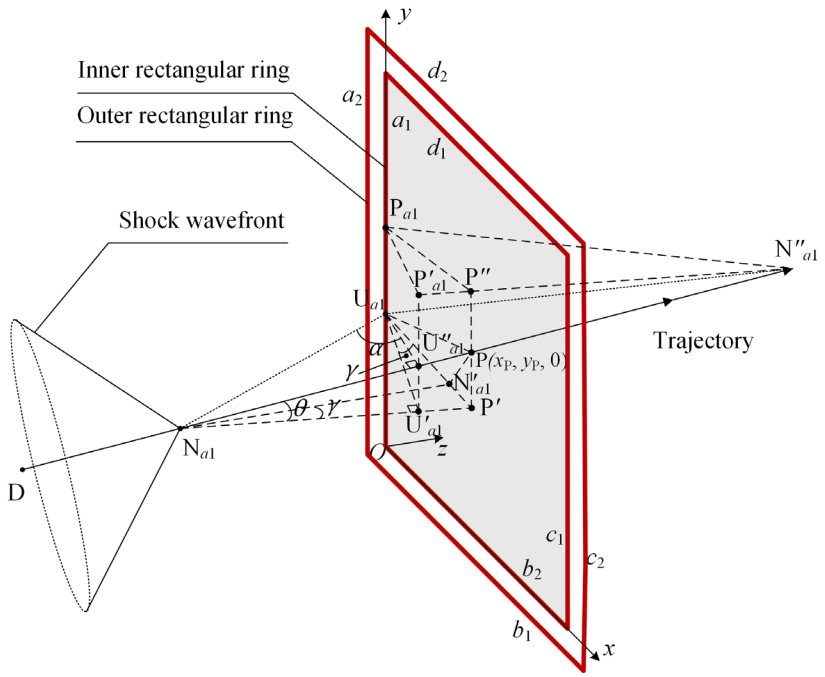

Figure 4. Schematic of the SW propagation process.

A perpendicular is drawn from N_{a1} to the measurement plane, with the foot of the perpendicular being N'_{a1}. Form P, a perpendicular to the x-axis, intersects the extension of the $U_{a1}N'_{a1}$ at P'_{a1}. A perpendicular is drawn from U_{a1} to the FO trajectory, with its foot denoted as U''_{a1}. From U_{a1}, a perpendicular is extended to the line segment $N_{a1}P'_{a1}$, with the foot of the perpendicular denoted as U'_{a1}. The angle between $N_{a1}N'_{a1}$ and $N_{a1}P'_{a1}$ is denoted as γ; the angle between $N_{a1}P$ and $N_{a1}P'_{a1}$ is θ; the angle between $U'_{a1}U_{a1}$ and $U_{a1}P'_{a1}$ is also γ; and the angle between $N_{a1}U_{a1}$ and $U_{a1}U''_{a1}$ is α. Let r_{a1} represent the distance $N_{a1}P$, and assume that the FO travels along $N_{a1}P$ at constant velocity. The horizontal distance from U_{a1} to point P, denoted as $U_{a1}P'_{a1}$, is $d_{a1} = x_P$. t_{a1} represents the SW propagation time along the shortest distance $N_{a1}U_{a1}$. It consists of two components: t_v, the time taken by the FO to travel along the trajectory DN_{a1}, and t_{c0}, the time taken for the SW generated at point N_{a1} to propagate to U_{a1}. Therefore, according to the time-equivalent model, t_{a1} can be expressed by

$$t_{a1} = t_v + t_{c0} = \frac{l}{v} + \frac{PU_{a1}}{v_{PUa1}} \tag{3}$$

In the $Rt\Delta PU_{a1}P'_{a1}$, $\cos\angle PU_{a1}P'_{a1} = 1/\sqrt{(1 + (k_{a1}\sin\theta)^2)}$; $v_{PUa1} = v_{x-}/\cos\angle PU_{a1}P'_{a1}$. At moment t_{a1}, it coincides with t'_{a1}, denoting the time at which the SW first reaches U_{a1}. It consists of two components: t_{DP}, the time taken by the FO to travel along trajectory DP, and

$t_{\mathrm{PU}a1}$, the time taken for the SW to propagate from point P to U_{a1} at its apparent velocity. Accordingly, in the RtΔPUa1P′, the decomposed minimum propagation time is given by

$$\begin{aligned} t_{a1} &= \frac{l}{v} + \frac{\mathrm{PU}_{a1}}{v_{\mathrm{PU}a1}} \\ &= \frac{l}{v} + \frac{\mathrm{PU}_{a1}\cos\angle\mathrm{PU}_{a1}\mathrm{P}'_{a1}}{v_{\mathrm{PU}a1}\cos\angle\mathrm{PU}_{a1}\mathrm{P}'_{a1}} \\ &= \frac{l}{v} + \frac{\mathrm{P}'_{a1}\mathrm{U}_{a1}}{v_{x-}} \\ &= \frac{l}{v} + \frac{d_{a1}}{v_{x-}} \end{aligned} \tag{4}$$

where in $\mathrm{Rt}\Delta\mathrm{U}'_{a1}\mathrm{U}_{a1}\mathrm{P}$, the ASWV v_{x-} is denoted as the direction a of the SW's apparent velocity in direction PU_{a1}. The fixed time l/v is present.

In the time-equivalent model, the known velocity parameters are limited to the flight velocity v of the FO, the shock-wave propagation speed c_0, and the apparent velocity v_h of the shock-wave in the direction perpendicular to its trajectory. In $\mathrm{Rt}\Delta\mathrm{N}_{a1}\mathrm{U}_{a1}\mathrm{U}''_{a1}$, the velocity on $\mathrm{U}_{a1}\mathrm{U}''_{a1}$ is $v_h = v\tan\alpha = c_{0/}\cos\alpha$.

On the FO's facing-away side, the trajectory line DP is extended to N''_{a1} such that $\mathrm{PN}''_{a1} = \mathrm{N}_{a1}\mathrm{P} = r_{a1}$. A perpendicular is drawn from N''_{a1} to point a_1, with its foot denoted as P_{a1}. From P_{a1}, a perpendicular is extended to the positive direction of the x-axis, intersecting the extension of line PP'_{a1} at P″.

Line $\mathrm{N}''_{a1}\mathrm{P}'''_{a1}$ is then constructed, and a perpendicular is dropped from it to intersect the extended line $\mathrm{U}'_{a1}\mathrm{U}''_{a1}$ at point P''_{a1}. In $\mathrm{Rt}\Delta\mathrm{P}''_{a1}\mathrm{P}_{a1}\mathrm{P}'''_{a1}$, $\angle\mathrm{P}''_{a1}\mathrm{P}_{a1}\mathrm{P}'''_{a1} = \gamma$ and $\mathrm{P}_{a1}\mathrm{P}'''_{a1} = d_{a1}$. In $\mathrm{Rt}\Delta\mathrm{P}'''_{a1}\mathrm{N}''_{a1}\mathrm{P}$, $\angle\mathrm{P}'''_{a1}\mathrm{N}''_{a1}\mathrm{P} = \theta$. In $\mathrm{Rt}\Delta\mathrm{P}'''_{a1}\mathrm{N}''_{a1}\mathrm{U}''_{a1}$, $\mathrm{N}''_{a1}\mathrm{U}''_{a1} = (r_{a1}\cos\theta + d_{a1}\sin\gamma)/\cos\theta$. In $\mathrm{Rt}\Delta\mathrm{N}''_{a1}\mathrm{U}_{a1}\mathrm{U}''_{a1}$, $\angle\mathrm{N}''_{a1}\mathrm{U}_{a1}\mathrm{U}''_{a1} = \alpha$ and $\mathrm{U}_{a1}\mathrm{U}''_{a1} = (r_{a1}\cos\theta + d_{a1}\sin\gamma)/\cos\theta\tan\alpha$. Finally, in $\mathrm{Rt}\Delta\mathrm{U}'_{a1}\mathrm{U}_{a1}\mathrm{P}$, the ASWV v_{x-} can be expressed as

$$v_{x-} = v_h \cdot \left| \frac{d_{a1}\cdot\cos\theta\tan\alpha}{r_{a1}\cos\theta + d_{a1}\sin\gamma} \right| \tag{5}$$

where v_{x-} is solely dependent on γ, θ, α, and c_0.

In $\mathrm{Rt}\Delta\mathrm{N}_{a1}\mathrm{U}_{a1}\mathrm{U}''_{a1}$ and $\mathrm{Rt}\Delta\mathrm{N}_{a1}\mathrm{U}_{a1}\mathrm{U}'_{a1}$, $\mathrm{N}_{a1}\mathrm{U}''_{a1} = (r_{a1}\cos\theta - d_{a1}\sin\gamma)/\cos\theta$ and $\mathrm{U}_{a1}\mathrm{U}''_{a1} = \mathrm{N}_{a1}\mathrm{U}''_{a1}/\tan\alpha$. Equation (4) was determined as follows:

$$\left(\mathrm{U}_{a1}\mathrm{U}'_{a1}\right)^2 + \left(\mathrm{N}_{a1}\mathrm{U}'_{a1}\right)^2 = \left(\mathrm{N}_{a1}\mathrm{U}''_{a1}\right)^2 + \left(\mathrm{U}_{a1}\mathrm{U}''_{a1}\right)^2 \tag{6}$$

The relationship between r_{a1} and d_{a1} is written as follows:

$$r_{a1} = d_{a1}\cdot\left(\frac{\sin\gamma}{\cos\theta} + \frac{\sin\alpha\cos\gamma}{\sqrt{1-\sin^2\alpha\cos^2\theta}}\right) = d_{a1}\cdot k_{a1} \tag{7}$$

where $\sin\alpha = c_0/v$; $k_{a1} = \sin\gamma/\cos\theta + \sin\alpha\cos\gamma/\sqrt{(1-\sin^2\alpha\cos^2\theta)}$.

The time taken by the FO to travel from the launch point to the measurement plane is assumed to be identical for all FOs. This travel time has no influence on the SW propagation toward the LOMs located on the DRR.

After updating the reference moment, t_{a1} can be written as

$$\begin{aligned} t'_{a1} &= \frac{d_{a1}}{v_{x-}} \\ &= \frac{d_{a1}}{v_h\cdot\left|\frac{d_{a1}\cdot\cos\theta\tan\alpha}{d_{a1}\cdot k_{a1}\cos\theta + d_{a1}\sin\gamma}\right|} \\ &= \frac{d_{a1}}{\frac{c_0}{\cos\alpha}\cdot\left|\frac{\cos\theta\tan\alpha}{k_{a1}\cos\theta+\sin\gamma}\right|} \end{aligned} \tag{8}$$

The arrival times of the SW at the remaining LOMs are similar to Equation (8).

2.4. IP Localization by Time-Equivalent Model

Based on the time-equivalent model of SW propagation, the ASWV v_{x-} in the same direction can be determined by measuring the time interval between the inner and outer rectangular rings. The ASWV component in a different direction can be derived by

$$\begin{cases} v_{x-} = \frac{S_{om}}{\Delta t_{a21}} \\ v_{x+} = \frac{S_{om}}{\Delta t_{c21}} \\ v_{y-} = \frac{S_{om}}{\Delta t_{b21}} \\ v_{y+} = \frac{S_{om}}{\Delta t_{d21}} \end{cases} \tag{9}$$

where $\Delta t_{a21} = t_{a2} - t_{a1}$, $\Delta t_{a21} = t_{a2} - t_{a1}$, $\Delta t_{a21} = t_{a2} - t_{a1}$, and $\Delta t_{a21} = t_{a2} - t_{a1}$ represent the time intervals in the *a*-, *b*-, *c*-, and *d*-directions, respectively.

In the *x*-direction, the time interval Δt_x, which is called the first arrive time of ASWV, is defined from the moment the FO reaches the IP at t_P until the first trigger occurs at the LOM in the *a*- or *c*-directions. Based on the relative size of $\Delta t_{ac1} = t_{a1} - t_{c1}$,

$$\begin{cases} l_{oa} = (v_{x-} + v_{x+})\Delta t_x + \Delta t_{ac1} \cdot v_{x-}, & \Delta t_{ac1} > 0 \\ l_{oa} = (v_{x-} + v_{x+})\Delta t_x - \Delta t_{ac1} \cdot v_{x+}, & \Delta t_{ac1} < 0 \end{cases} \tag{10}$$

Δt_x can be calculated as

$$\begin{cases} \Delta t_x = \frac{l_{om} - \Delta t_{ac1} \cdot v_{x-}}{v_{x-} + v_{x+}}, & \Delta t_{ac1} > 0 \\ \Delta t_x = \frac{l_{om} + \Delta t_{ac1} \cdot v_{x+}}{v_{x-} + v_{x+}}, & \Delta t_{ac1} < 0 \end{cases} \tag{11}$$

In the *y*-direction, Δt_x is calculated analogously.

The IP can be calculated using

$$\begin{cases} \begin{cases} x = v_{x-} \cdot \Delta t_x \\ y = v_{y-} \cdot \Delta t_y \end{cases} & , \Delta t_{ac1} < 0, \Delta t_{bd1} < 0 \\ \begin{cases} x = v_{x-} \cdot \Delta t_x \\ y = l_{om} - v_{y+} \cdot \Delta t_y \end{cases} & , \Delta t_{ac1} < 0, \Delta t_{bd1} > 0 \\ \begin{cases} x = l_{om} - v_{x+} \cdot \Delta t_x \\ y = v_{y-} \cdot \Delta t_y \end{cases} & , \Delta t_{ac1} > 0, \Delta t_{bd1} < 0 \\ \begin{cases} x = l_{om} - v_{x+} \cdot \Delta t_x \\ y = l_{om} - v_{y+} \cdot \Delta t_y \end{cases} & , \Delta t_{ac1} > 0, \Delta t_{bd1} > 0 \end{cases} \tag{12}$$

3. Experimental Setup of Localization Method

The overall experimental setup is illustrated in Figure 5: (a) the topological schematic and (b) the physical diagram of the dual rectangular ring schematic of the DRRLOMA. The DRRLOMA system consists of five components: a dual rectangular ring, a signal acquisition instrument, a DRRLOMA power module, signal conditioners, and a time-difference calculating device (all from Xi'an, China). The dual rectangular ring is fixed on the DRRLOMA mount. The inner ring comprises four LOM units, with two arranged mutually orthogonally. The separation between the transmitter and receiver of one unit is defined as l_x, and that of the other unit is l_y. The remaining two LOM units are arranged similarly. The outer ring contains four LOM units in the same configuration but positioned outward. Both rings lie in the measurement plane for IP dispersion evaluation. Positions 1

and 2 correspond to the inner and outer rings. The LOM units on the left and bottom sides of the inner ring define x- and y-axes, respectively, with their intersection as the origin o of o-xyz. In the xoy plane, the a-, b-, c-, and d-directions correspond to the negative x-axis, negative y-axis, positive x-axis, and positive y-axis, respectively. The signal acquisition instrument uses threshold voltage comparison for SW-affected analog signals. The time-difference calculating device computes the time difference between the reference moment and SW arrival times at the LOM units as t_{a1}, t_{a2}, t_{b1}, t_{b2}, t_{c1}, t_{c2}, t_{d1}, and t_{d2}. Figure 5a illustrates the cable layout configuration, where distinct colors represent different cable types: orange denotes power supply cables, dark blue indicates analog signal cables, and light blue represents digital signal cables. This color-coded scheme facilitates clear identification and analysis of the signal transmission paths within the system.

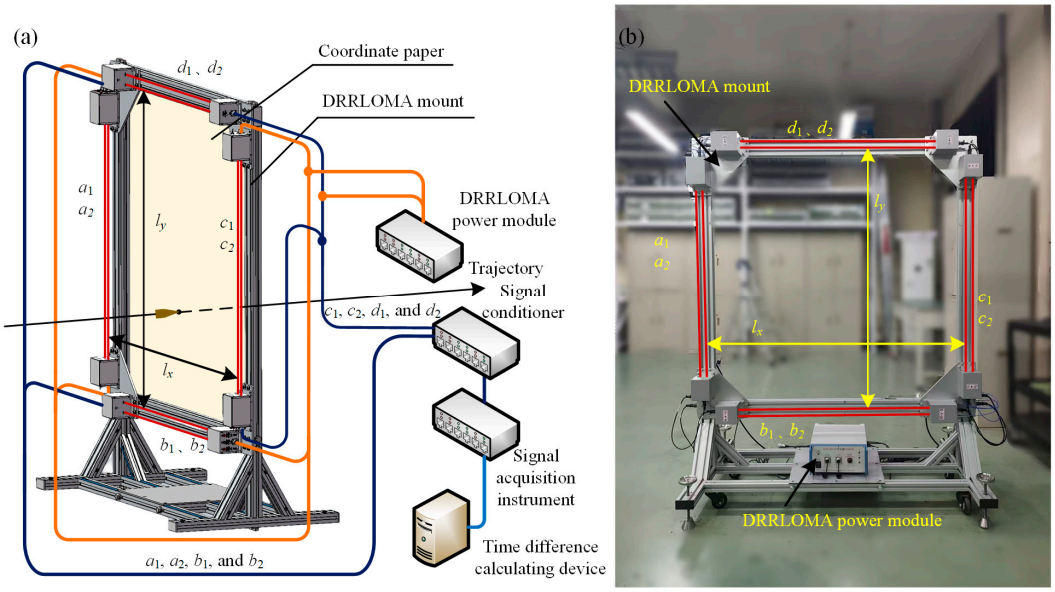

Figure 5. DRRLOMA localization system: (**a**) the topological schematic and (**b**) the dual rectangular ring schematic of the DRRLOMA.

4. Results and Discussion

4.1. Analysis of Localization Error

Based on the error propagation formula, the coordinate measurement error is analyzed and calculated. Due to the symmetry between the x- and y-directions, the analysis is illustrated using the x-coordinate measurement formula as an example. By taking the total differential of the x-coordinate formula for the IP, the corresponding error expression is obtained by

$$\begin{cases} |dx| \le \left|\frac{\partial x}{\partial v_{x+}} dv_{x+}\right| + \left|\frac{\partial x}{\partial \Delta t_x} d\Delta t_x\right| & , \Delta t_{ac1} < 0 \\ |dx| \le \left|\frac{\partial x}{\partial l_{om}} dl_{om}\right| + \left|\frac{\partial x}{\partial v_{x-}} dv_{x-}\right| + \left|\frac{\partial x}{\partial \Delta t_x} d\Delta t_x\right| & , \Delta t_{ac1} > 0 \end{cases} \tag{13}$$

where dv_{x-} and dv_{x+} represent the errors in ASWV. $d\Delta t_x$ denotes the timing error associated with Δt_x, and dl_{om} corresponds to the measurement error of the side length of the inner rectangular ring.

Taking the total differential of v_{x-} yields the following expression:

$$\begin{aligned} |dv_{x-}| &\le \left|\frac{\partial v_{x-}}{\partial S_{om}} dS_{om}\right| + \left|\frac{\partial v_{x-}}{\partial \Delta t_{a21}} d\Delta t_{a21}\right| \\ &\le \left|\frac{1}{\Delta t_{a21}} dS_{om}\right| + \left|-\frac{S_{om}}{\Delta t_{a21}^2} d\Delta t_{a21}\right| \end{aligned} \tag{14}$$

where dS_{om} represents the measurement error in the spacing distance between the inner and outer rectangular ring, expressed as dS_{om} = 0.3 mm + 0.2S_{om} mm [10].

Taking the total differential of v_{x+} yields the following expression:

$$\begin{aligned} |dv_{x+}| &\le \left|\frac{\partial v_{x+}}{\partial S_{om}} dS_{om}\right| + \left|\frac{\partial v_{x+}}{\partial \Delta t_{c21}} d\Delta t_{c21}\right| \\ &\le \left|\frac{1}{\Delta t_{c21}} dS_{om}\right| + \left|-\frac{S_{om}}{\Delta t_{c21}^2} d\Delta t_{c21}\right| \end{aligned} \tag{15}$$

Taking the full differential of Δt_x yields the following expression:

$$\begin{cases} |d\Delta t_x| \le \left|\frac{1}{v_{x-}+v_{x+}} dl_{om}\right| + \left|-\frac{v_{x+}}{v_{x-}+v_{x+}} d\Delta t_{ac1}\right| \\ \quad + \left|\left(\frac{\Delta t_{ac1}}{v_{x-}+v_{x+}} - \frac{l_{om}+v_{x+}\Delta t_{ac1}}{(v_{x-}+v_{x+})^2}\right) dv_{x+}\right| \quad , \Delta t_{ac1} < 0 \\ \quad + \left|\left(-\frac{l_{om}+v_{x+}\Delta t_{ac1}}{(v_{x-}+v_{x+})^2}\right) dv_{x-}\right| \\ |d\Delta t_x| \le \left|\frac{1}{v_{x-}+v_{x+}} dl_{om}\right| + \left|-\frac{v_{x-}}{v_{x-}+v_{x+}} d\Delta t_{ac1}\right| \\ \quad + \left|\left(-\frac{\Delta t_{ac1}}{v_{x-}+v_{x+}} - \frac{l_{om}-v_{x-}\Delta t_{ac1}}{(v_{x-}+v_{x+})^2}\right) dv_{x-}\right| \quad , \Delta t_{ac1} > 0 \\ \quad + \left|\left(-\frac{l_{om}-v_{x-}\Delta t_{ac1}}{(v_{x-}+v_{x+})^2}\right) dv_{x+}\right| \end{cases} \tag{16}$$

For $S_{om} \in$ [1 mm, 50 mm], assuming a fixed timing error of Δt = 0.5 µs, the effect of varying S_{om} and dt is analyzed, as shown in Figure 6a. Similarly, for $\Delta t \in$ [0.1 µs, 10 µs], assuming a fixed spacing of S_{om} = 30 mm, the effect of varying dt is analyzed, as shown in Figure 6b. MATLAB R2022a served as the simulation platform for generating the results in Figure 6.

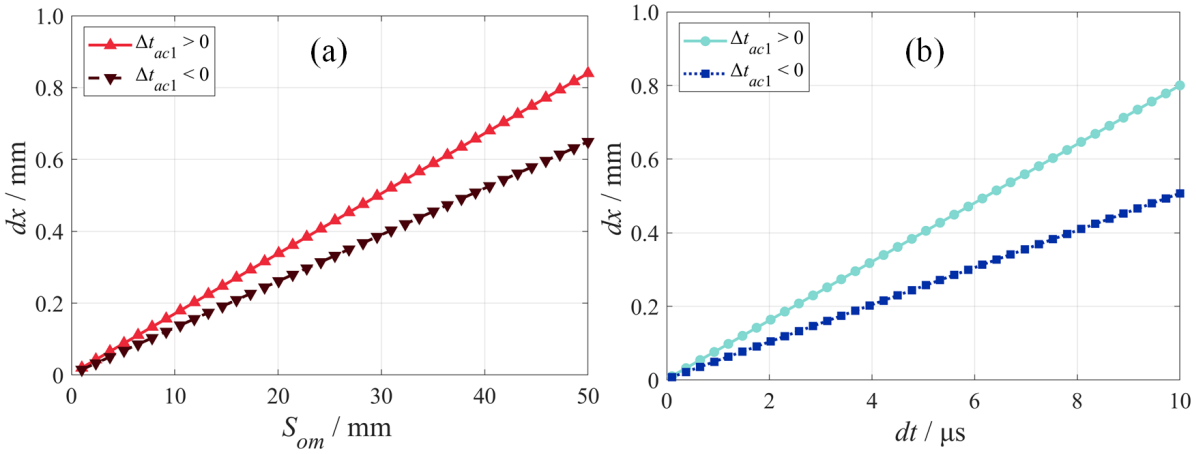

Figure 6. Variation law of coordinate errors: (**a**) effect of S_{om} on dx; (**b**) effect of dt on dx.

In summary, both S_{om} and dt exhibit a linear influence on dx, with dx increasing as either parameter increases. When S_{om} < 30 mm, the resulting error satisfies dx < 0.5 mm. Similarly, when dt < 6 µs, the error also remains below 0.5 mm.

The localization error associated with $\Delta t_{ac1} > 0$ is observed to be larger than that associated with $\Delta t_{ac} < 0$. This behavior arises from the inclusion of an additional term $|\partial x/\partial l_{om} \cdot dl_{om}|$ in the error propagation process, which results in a relatively conservative estimation of the localization error. Despite this, the resulting error remains below 0.5 mm for the specified parameter range.

4.2. LOM Experimental Results

Experiments conducted with the LOM verified its performance ("A experiment") and analyzed the potential for extending the DRRLOMA's LOM configuration to a 10 m ("B experiment and C experiment"). LOM experiments were conducted to investigate the variation in the max of the LOM output voltage with increasing SW propagation distance. An electric spark generator was employed as the shock-wave source, with a rated voltage of 10 kV and a rated current of 100 mA. The analog output voltage waveforms of the LOM were acquired using an oscilloscope. Based on multiple live-fire tests, we found that the SW generated by the electrical spark source with the parameters described above exhibits a high degree of similarity to the SW produced by a 7.62 mm-diameter FO.

The A experiment of the LOM is as follows: The LOM transmitter and receiver were arranged in a face-to-face configuration with a separation distance of 2 m. The experimental setup is schematically illustrated in Figure 7a. The acquired analog waveforms were fitted, and the resulting curve is shown in Figure 7b. Furthermore, the experimental results were compared with predictions from an empirical formula [42] and the results reported in ref. [43]. The results indicate that the amplitude of the LOM analog output voltage gradually decreases as the shock-wave propagation distance increases. Furthermore, as indicated by the curve variations in Figure 7, the sensitivity of the LOM is higher than that reported in ref. [43].

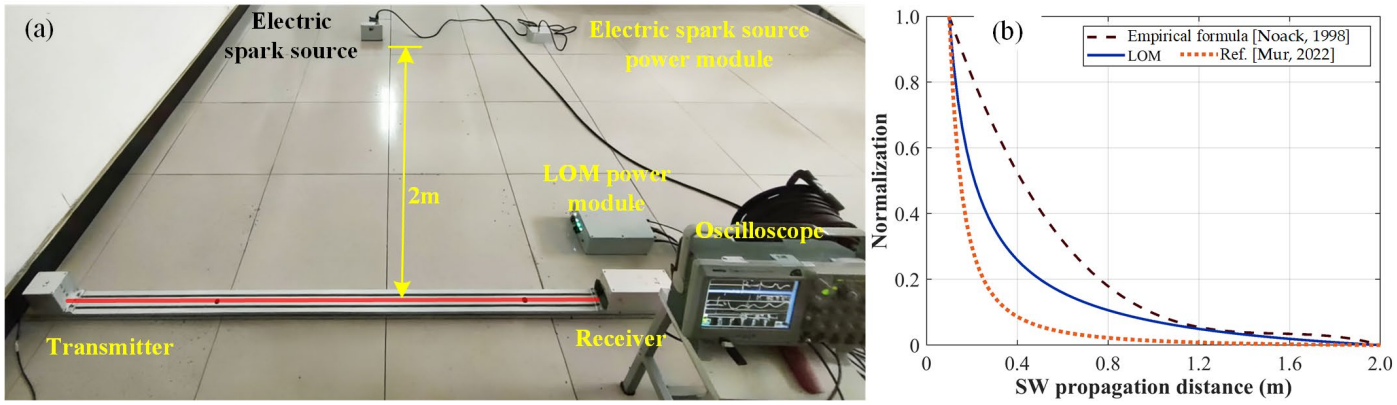

Figure 7. (**a**) Schematic of the LOM experiments. (**b**) Variation curve of the LOM output signal as the SW propagation distance increases and comparison curves (The data from the LOM are plotted as a solid line, while predictions from the empirical formula [42] and ref. [43] are represented by dashed and dotted lines, respectively).

The B experiment of the LOM is as follows: An electric spark generator was placed 12 m away from the LOM laser path, which has a length of 2 m, inside the laboratory. The experimental layout is shown in Figure 8a. The SW signals acquired by the LOM are presented in Figure 8b. In Figure 8b, the max amplitude recorded by the LOM reached 9.59 V. Despite the attenuation of SWs during indoor propagation, the successful acquisition of these signals confirms the capability of the LOM to perform SW measurements at a range of 12 meters. This result also demonstrates the sufficient detection sensitivity of the LOM. The experiment described above also provides an engineering basis for the development of the 10 m $\times$ 10 m measurement plane. Therefore, the proposed configuration for a 10 m $\times$ 10 m measurement plane is deemed feasible.

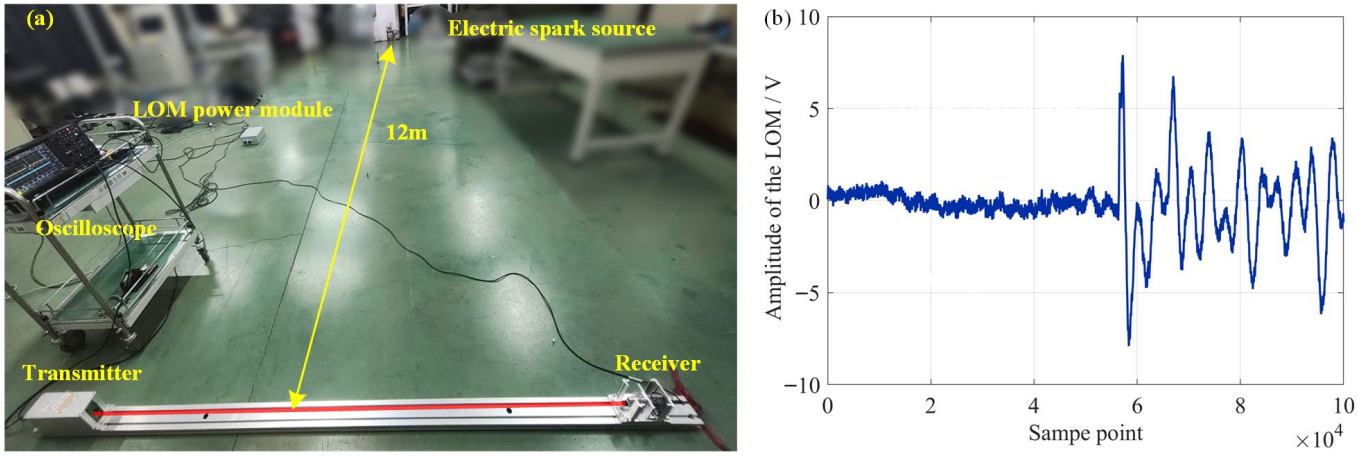

Figure 8. (**a**) Schematic diagram of SW at 10 m measured by the 2 m LOM. (**b**) The waveform of the LOM.

The C experiment of the LOM is as follows: In a T-shaped corridor, each orthogonal arm had a uniform width of 2.4 m. An electric spark generator, serving as the SW source, was positioned 12 m away from the LOM's laser path, whose length was 12 m. The system topology is illustrated in Figure 9a, while photographs of the experimental setup from the two orthogonal directions are provided in Figure 9b and c, respectively. The LOM successfully detected the SW signal, as shown in the acquired waveform in Figure 9d, where a max amplitude of 9.78 V was recorded. The successful detection of an SW at a 12 m standoff distance by this 12 m-long LOM validates its core detection capability and confirms its adequate sensitivity. Thus, this experiment further substantiates the feasibility of constructing a large-scale 10 m × 10 m measurement plane.

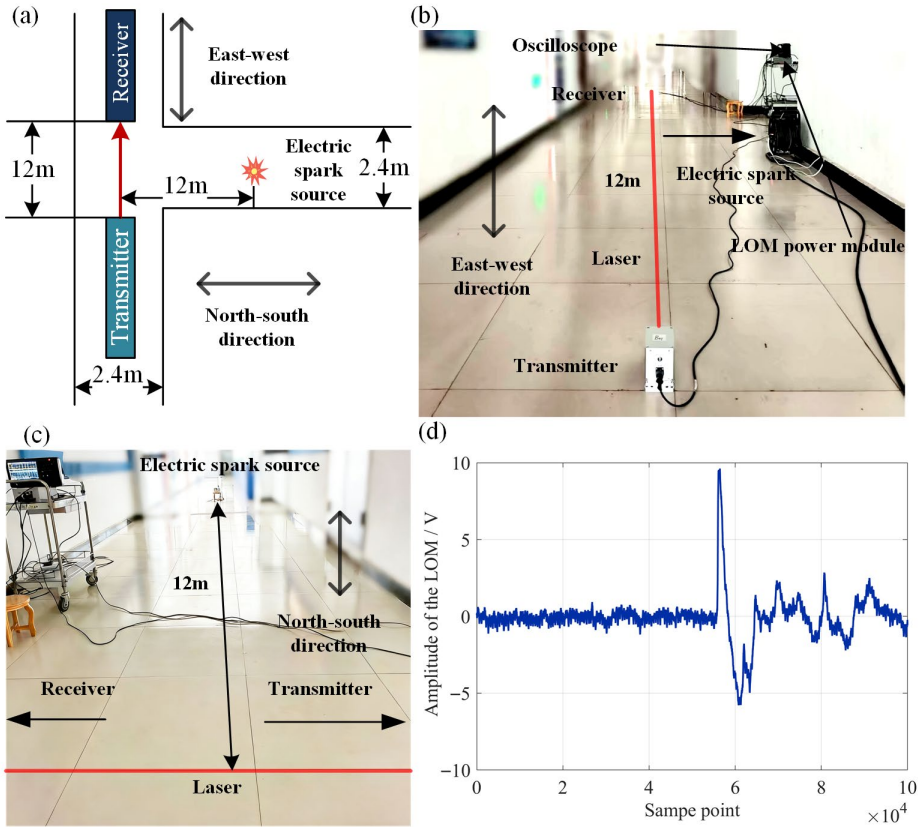

Figure 9. (**a**) Schematic of a T-shaped corridor; (**b**) schematic of the 10 m LOM in east–west direction. (**c**) Schematic of SW at 10 m measured by LOM's laser in north–south direction. (**d**) The waveform of the LOM.

4.3. DRRLOMA Localization Experimental Results

The setup for the experiment is shown in Figure 5. A 1 m × 1 m effective measurement area was established in the experiment, matching the area of the inner rectangular ring. A 5.8 mm-diameter FO was used for the experiment. Figure 10 illustrates the BSW signals acquired by a_1-LOM and a_2-LOM of the DRRLOMA in one experimental trial. In the waveform, the first rising edge of each channel indicates the arrival of the BSW, while the subsequent irregular signals are likely reflections of the BSW from surrounding walls. Table 1 lists the LOM output time differences measured within the DRRLOMA (in ms).

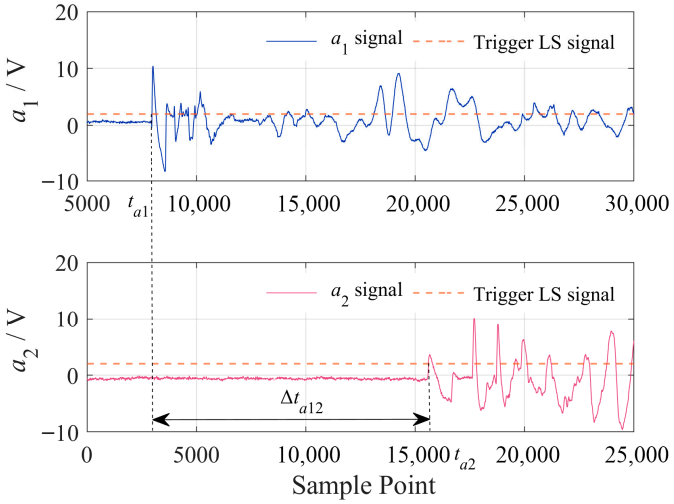

Figure 10. Waveform of the SW arriving at the DRRLOMA.

Table 1. Time difference in the SWs arriving at the DRRLOMA (ms).

No.	Δt_{a1}	Δt_{a2}	Δt_{b1}	Δt_{b2}	Δt_{c1}	Δt_{c2}	Δt_{d1}	Δt_{d2}
1	0.079	0.271	0.084	0.304	1.398	1.544	0.165	0.182
2	1.311	1.448	1.656	2.057	0.146	0.471	0.795	0.930
3	0.858	1.073	0.732	0.875	1.003	1.170	0.969	1.166
4	1.014	1.217	1.132	1.358	1.695	2.034	1.359	1.631
5	1.872	2.244	1.438	1.588	0.748	0.899	1.993	6.717
6	2.136	2.358	1.998	2.205	0.098	0.375	2.208	8.291
7	0.212	0.317	0.349	0.520	3.235	3.641	0.776	0.874
8	2.852	3.209	0.661	0.995	0.252	0.377	0.201	0.226
9	0.742	1.128	3.389	3.810	1.069	1.202	2.572	3.882
10	1.763	1.982	1.090	1.229	0.529	0.802	1.621	2.388
11	2.772	3.119	0.3506	0.528	0.260	0.389	0.660	0.662
12	0.783	1.190	2.998	3.371	0.911	1.024	2.435	2.436
13	1.342	1.508	2.314	2.608	0.554	0.838	1.971	1.973

According to the shock-wave arrival times in Table 1, and by applying the time-equivalent model in conjunction with Equations (9)–(12), the localization coordinates of the FO were calculated. These coordinates are analyzed to evaluate the positioning errors introduced during the experimental procedure, providing a basis for subsequent comparisons with the localization errors of different sensors. The measurement error of the IP is expressed as

$$\delta_{xy} = \frac{\sum_{n=1}^{10} \sqrt{(|x_{P1}| - |x_{s1}|)^2 + (|y_{P1}| - |y_{s1}|)^2}}{10} \quad (17)$$

where (x_s, y_s) represents the IP recorded on the coordinate paper, and (x_P, y_P) represents the results calculated using the IP method described in this paper. The measured coordinates (x_s (1), y_s (1)) and calculated coordinates (x_P (1), y_P (1)) of the first object serve as reference points. Subtracting these reference values yields the relative coordinates ($|x_{s1}|$, $|y_{s1}|$) and ($|x_{P1}|$, $|y_{P1}|$) for each shot. The results (in millimeters) are summarized in Table 2.

Table 2. IP calculation results (mm).

No.	x_s	y_s	$\|x_{s1}\|$	$\|y_{s1}\|$	x_P	y_P	$\|x_{P1}\|$	$\|y_{P1}\|$	δ_{xy}
1	247.0	252.8	0.0	0.0	246.84	252.55	0.00	0.00	0.00
2	255.9	504.0	9.0	251.2	255.92	503.99	9.08	251.44	0.28
3	242.8	744.1	4.1	491.3	242.86	744.05	3.99	491.50	0.28
4	503.0	252.7	256.0	0.2	502.99	252.82	256.14	0.27	0.31
5	492.1	504.0	245.1	251.1	492.01	504.00	245.17	251.45	0.31
6	497.0	744.0	250.1	491.2	497.03	744.03	250.19	491.48	0.32
7	751.1	252.8	504.1	0.0	751.18	252.68	504.33	0.13	0.26
8	745.0	504.0	498.0	251.2	744.93	503.98	498.08	251.43	0.26
9	752.9	744.0	506.0	491.2	752.96	744.00	506.12	491.46	0.29
10	378.0	375.9	131.0	123.1	377.99	375.96	131.15	123.41	0.31
11	371.9	628.0	124.9	375.2	371.93	628.00	125.09	375.45	0.30
12	620.9	325.9	374.0	73.1	620.91	325.89	374.06	73.34	0.26
13	629.0	628.0	382.1	375.2	629.08	628.03	382.24	375.48	0.31
				Mean					0.28
				Standard deviation (SD)					0.22

Figure 11 presents the localization error values δ_{xy} corresponding to the IP coordinates (x_P, y_P) listed in Table 2, evaluated at their respective spatial positions. In addition, interpolation-based fitting was applied to the remaining points to obtain the spatial distribution of the localization error over the measurement plane. The results reveal that the localization error of the IP is relatively uniform in the central region of the measurement plane. This suggests that when the FO impacts within the central area, the localization error remains small and stable. Furthermore, the error distribution shown in Figure 11, which is larger in the center and smaller in the periphery, is primarily caused by temporal errors. As shown in Figure 7b, when an IP is closer to the LOM, the shock-wave intensity increases. This leads to more accurate identification of the characteristic arrival time of the shock signal and a reduction in the time delay between the two measurement channels. Conversely, for IPs located in the central region, the intensity of the shock-wave reaching the LOM diminishes. Consequently, the identification of the characteristic arrival time becomes less accurate compared to the former case, resulting in an increased inter-channel time delay.

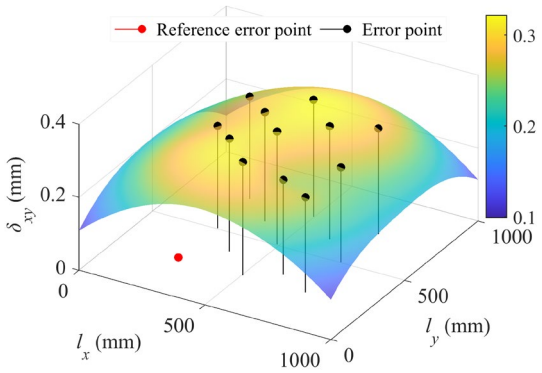

Figure 11. Error distribution of IP localization.

4.4. Discussion of Experimental Results

Using a DRRLOMA for FO localization, the FO impacts the measurement surface at varying incident angles in experiments. The results indicate that when the FO impact occurs in the central region, the localization error is relatively stable. Overall, both the mean and SD remain below 0.5 mm. In this study, the ratio error—defined as the coordinate measurement error relative to the measurement area—is 0.5‰ (0.5 mm in a 1 m × 1 m plane). To comprehensively evaluate the performance of the proposed method, Table 3 provides a quantitative comparison with results reported in prior studies across several key metrics. These metrics include measurement plane size, localization error, error rate, sensing shape, computational complexity, real-time capability, cost-effectiveness, primary advantages, and primary limitations.

In terms of localization accuracy and the FO's incidence model, the DRRLOMA achieves a positioning error of 0.5 mm on a 1.0 m × 1.0 m measurement plane, with a relative error of 0.5‰. This represents a twentyfold increase in accuracy compared to the acoustic sensor array and a sevenfold increase over the multi-light-screen array, highlighting the superior error suppression capability of the analytical approach based on the time-equivalent model. Regarding the geometric form of their constituent sensing units, the three systems differ as follows: the DRRLOMA employs a linear array, acoustic sensor arrays utilize dot-like nodes, and multi-light-screen arrays constitute a planar configuration. In terms of sensing complexity, the DRRLOMA occupies an intermediate position between the other two systems.

Table 3. Comparison of results.

Sensor Type	DRRLOMA	Acoustic Sensors [25]	Multi-Light-Screen Array [44]
Area	1.0 m × 1.0 m	1.0 m × 1.0 m	2.0 m × 2.0 m
Errors	0.5 mm	10.0 mm	3.5 mm
Ratio Error	0.5‰	10.0‰	1.8‰
Sensing shape	Linear	Dot	Plane
Computational Complexity	Multi-channel signal processing; positioning computed via concise formulas	Multi-channel signal processing via modest complexity formulas	Multi-channel signal processing via significant complex formulas
Real-Time Capability	Response times of less than 500 ms can be achieved by hardware; good real-time performance		
Cost-Effectiveness Analysis	Moderate initial cost (including the sensor structures and hardware circuitry, etc.)	Low initial cost	High initial cost
Primary Advantages	High accuracy, easy scalability (10 m ×10 m), and sound speed calibration-free computation process	Low cost; well-established technology.	Good environmental adaptability; high accuracy; no velocity constraint
Primary Limitations	Supersonic FO requirement	Supersonic FO requirement; sound speed calibration requirement	High initial cost; limited scalability of the measurement plane

Regarding computational efficiency and real-time performance, the DRRLOMA utilizes the TDOA from eight LOM channels, which are directly input into concise geometric

analytical formulas to calculate the position. This results in low computational complexity, endowing it with a robust real-time processing capability. In comparison, acoustic sensor arrays rely on analytical formulas of modest complexity, whereas multi-light-screen arrays depend on those of significant complexity. Although both methods are inferior to the DRRLOMA in terms of computational efficiency, they can achieve comparable real-time performance through hardware optimization.

In terms of cost-effectiveness, although the DRRLOMA employs LOM units with a higher unit cost, its total cost remains intermediate among the three methods. Furthermore, the system delivers high positioning accuracy, offers easy scalability (e.g., to a 10 m $\times$ 10 m area), and features a computation process that does not require sound speed calibration. In contrast, acoustic sensor arrays benefit from a low initial cost and are based on well-established technology. However, they require dense sensor deployment and are susceptible to environmental interference. Multi-light-screen arrays, which utilize high-precision optical components and involve demanding installation and alignment procedures, entail a high initial investment.

In summary, both the DRRLOMA and acoustic sensor arrays require the FO to be supersonic for effective operation. The restriction of the multi-light-screen arrays is the limited scalability of the measurement plane, compounded by a high initial cost. The DRRLOMA method achieves a batter balance between accuracy, real-time performance, and overall cost-effectiveness. It is particularly well-suited for the localization of supersonic FOs in scenarios that impose stringent requirements on measurement reliability, response speed, and long-term operational stability.

4.5. Discussion for Engineering Deployment and Application

The field deployment of the DRRLOMA method presents several practical engineering challenges that must be addressed. Here, we discuss the key considerations as follows:

(a) Robustness to Environmental Factors: In the DRRLOMA, the LOMs make the system unsusceptible to environmental variables. Variations in environmental factors, such as temperature, humidity, and density, affect the propagation of the SW through the medium but do not influence the laser sensing path of the LOM. Once calibrated, the LOM in the DRRLOMA—provided that the transmitter and receiver remain aligned and no shock-wave interference from other FOs is present—generates a transient signal exclusively when a shock-wave arrives at its laser path. Otherwise, the system remains in a ready state. However, extreme turbulent airflow directly impinging on the laser paths could cause signal scintillation, a topic for future investigation in harsh environments.

(b) System Calibration Strategy: The proposed calibration strategy involves three levels. The first addresses the fixed geometric parameters of the DRRLOMA structure, such as side lengths and orthogonality, which are precisely measured using theodolites and auxiliary lasers. Second, the laser beams between the transmitter and receiver of each LOM must be accurately aligned, which is critical for achieving precise FO localization. Third, since the DRRLOMA localization algorithm does not depend on environmental sound speed, no prior sound speed calibration is required. Additionally, the symmetry of the dual-rectangular-ring structure simplifies the calibration process.

(c) Long-Term Stability Considerations: Once the structural frame of the DRRLOMA is fabricated to its specified dimensions, it exhibits excellent mechanical stability suitable for long-term deployment. The hardware circuitry has been tested for electromagnetic interference resistance as well as performance under low-temperature and high-humidity conditions, confirming its long-term stability. Furthermore, solid-state laser diodes (940 nm) and photodetectors (940 nm) integrated into the LOM exhibit long-

term stability features with high reliability, long lifetime, and low output drift. As illustrated in Figure 5b, the fully assembled DRRLOMA functions as a single, rigid sensing module with robust resistance to vibration.

5. Conclusions

In this study, a novel IP localization method based on a DRRLOMA was proposed and validated. By introducing the time-equivalent model and constructing a DRRLOMA composed of eight LOMs, the proposed approach effectively addresses the challenge of IP positioning under oblique impact conditions, particularly when the velocity vector of the FO is not aligned with the normal of the measurement plane and significant impact dispersion is present. Unlike conventional point-based acoustic sensor arrays, which suffer from limited spatial sampling capability and reduced localization accuracy, the proposed method employs LOM-based optical measurement units to form a well-defined measurement plane. By extending the laser paths closer to the SW source generated by the FO, higher-intensity SW signals can be acquired, thereby enhancing the robustness and accuracy of IP localization. Both theoretical error analysis and experimental validation demonstrate strong consistency, with the localization error remaining below 0.5 mm. Compared with existing IP positioning approaches, the proposed DRRLOMA-based system achieves higher measurement precision while maintaining a significantly lower system cost, highlighting its practical applicability and scalability. Although the experimental validation in this study is confined to a 1 m $\times$ 1 m measurement plane due to laboratory constraints, the method can be readily extended to larger areas (e.g., 10 m $\times$ 10 m) by appropriately increasing the distance between the transmitter and receiver ends of the LOM, ensuring their alignment, and securing the assembly on a newly constructed 10 m $\times$ 10 m mount.

Future work will further investigate the influence of key parameters, including the distance between the LOM and the FO's trajectory, as well as the LOM length l, on time-delay characteristics and positioning accuracy, thereby providing a more comprehensive understanding of system performance.

Author Contributions: Conceptualization, C.D. and J.N.; methodology, C.D. and J.N.; validation, Y.W. and J.L.; formal analysis, Y.W.; investigation, C.D.; resources, Y.W. and J.L.; data curation, C.D.; writing—original draft preparation, C.D.; writing—review and editing, C.D. and J.N.; visualization, C.D.; supervision, J.N.; project administration, H.T.; funding acquisition, J.N. All authors have read and agreed to the published version of the manuscript.

Funding: The authors would like to acknowledge the National Natural Science Foundation of China (Grant No. 61471289), which provided funds for conducting experiments.

Institutional Review Board Statement: Not applicable.

Informed Consent Statement: Not applicable.

Data Availability Statement: The authors confirm that the data supporting the findings of this study are available within the article.

Conflicts of Interest: The authors declare no conflicts of interest.

Abbreviations

FO	Flying object
IP	Impact point
LS	Light screen
CCD	Charge-coupled device
SW	Shock-wave

TDOA	Time difference of arrival
DRRLOMA	Dual-rectangular-ring linear optical microphone array
LOM	Linear optical microphone
ASWV	Apparent shock-wave velocity

References

1. Chinke, S.L.; Berhe, S.; Alegaonkar, P.S. High Speed Flying Object Sensor: Design, Development and System Engineering. *IEEE Sens. J.* **2021**, *21*, 27062–27068. [CrossRef]
2. Li, H.; Lei, Z. Measurement of Flying object Burst Coordinates by Using Multi-Screen Optical Method and Its Error Analysis. *Acta Opt. Sin.* **2012**, *32*, 0212003. [CrossRef]
3. Feng, B.; Shi, X. Studies of acoustic target with two equilateral triangle arrays. *Appl. Acoust.* **2012**, *31*, 140–144. [CrossRef]
4. Lin, Y.; Di, C.; Di, C.; Gong, X.; Ji, H. Location model of oblique incident double triangular array based on shock propagation path. *Acta Armamentarii* **2019**, *40*, 251–256. [CrossRef]
5. Zou, Y.; Zhang, L.; Wang, H. Numerical Simulation of Dispersion of Flying object Jump Caused by Initial Disturbance. *J. Ordnance Equip. Eng.* **2020**, *41*, 46–52. [CrossRef]
6. de Cêa, B.S.A.; Pereira Junio, R.F.; Silva, D.S.; da Costa Garcia Filho, F.; Monteiro, S.N.; Cassiano Nascimento, L.F. An experimental and numerical study of the ballistic behavior of an epoxy matrix hybrid composite reinforced with aramid fabric and fique fabric. *J. Mater. Res. Technol.* **2025**, *35*, 2037–2054. [CrossRef]
7. Shen, Y.Z.; Wen, K.Y.; Shen, Y.L.; Luo, X.H.; Nie, W.X.; Wang, H.C.; Xu, H.R. Dynamic Response and Energy Absorption Characteristics of Auxetic Concave Honeycomb Pad for Ballistic Helmet under Shock Wave and Bullet Impact. *Mech. Solids* **2025**, *59*, 3050–3067. [CrossRef]
8. Tang, E.L.; Liang, Z.Q.; Wang, L.; Han, Y.F. Experimental investigations on location of debris impact source based on acoustic emission. *Adv. Space Res.* **2019**, *64*, 2390–2404. [CrossRef]
9. Liu, M.; Wang, Q.; Zhang, Q.; Long, R.; Su, Z. Characterizing hypervelocity (>2.5 km/s)-impact-engendered damage in shielding structures using in-situ acoustic emission: Simulation and experiment. *Int. J. Impact. Eng.* **2018**, *111*, 273–284. [CrossRef]
10. Tian, H.; Ni, J. Research on measuring method for terminal trajectory of the flying object parameters by nine-light-screens-array. *Chin. J. Sci. Instrum.* **2018**, *39*, 17–23. [CrossRef]
11. Li, H.; Ni, J.; Yang, X.; Chen, D. Research on Attenuation Motion Test Based on Double-N Six-Light-Screen System. *Photonics* **2022**, *9*, 516. [CrossRef]
12. Li, H. An Optical Transformation Design Method of Sky Screen Sensor Based on Lens Convergence. *IEEE Sens. J.* **2024**, *24*, 40685–40695. [CrossRef]
13. Li, H.; Li, X.; Zhang, X.; Lu, L. Design of Photoelectric Detection Sensor Incorporated with Meso-Lens Array and Its Detection Screen Performance Analysis. *IEEE Sens. J.* **2020**, *21*, 1444–1452. [CrossRef]
14. Geng, D.; Chen, L.; Hou, Z.; Zhang, X.; Wei, X. The laser screen imaging measurement system based on arrayed fibers. *Opt. Lasers Eng.* **2024**, *183*, 108551. [CrossRef]
15. Chen, R.; Cai, R.; Ji, B. Flying object flight parameters measurement method based on the spatial distribution of light-screen thickness. *Measurement* **2022**, *195*, 111143. [CrossRef]
16. Li, H.; Zhang, X.; Gao, J. A Design Method of Active Photoelectric Detection Sensor Based on 1-D Multiunit p-i-n Detector and Its Detection Model. *IEEE Sens. J.* **2022**, *22*, 21600–21612. [CrossRef]
17. Li, H.; Zhang, X. Laser Reflection Characteristics Calculation and Detection Ability Analysis of Active Laser Detection Screen Instrument. *IEEE Trans. Instrum. Meas.* **2021**, *71*, 7000111. [CrossRef]
18. Liu, X.; Lei, Z. Measurement method of flying object explosion position based on two area array CCDs intersection and its error analysis. In *2023 9th International Conference on Mechanical and Electronics Engineering (ICMEE)*; IEEE: New York, NY, USA, 2023; Volume 2023, pp. 17–19. [CrossRef]
19. Li, H.; Zhang, X.; Miao, W. Spatial Position Measurement of Multiple Targets Using a Line Lasers and a Plane Array Camera. *IEEE Sens. J.* **2019**, *19*, 10443–10451. [CrossRef]
20. Duan, C.; Ni, J.; Li, J.; Chen, R.; Cui, C.; Liu, Y. Spatial distribution of sensitivity of large-area triangular detection light screen. *J. Appl. Opt.* **2021**, *42*, 956–962. [CrossRef]
21. Duan, C.; Sun, Z.; Li, H.; Ni, J.; Wu, Z. Sensitivity distribution of large-area triangular detection light screen with original reflection. *J. Appl. Opt.* **2023**, *44*, 113–121. [CrossRef]
22. Zengin, K.; Yeşildirek, A. A Hybrid Model for 3-D Gunshot Localization Using Muzzle Blast Sound Only. *IEEE Trans. Instrum. Meas.* **2024**, *73*, 2533810. [CrossRef]
23. Chen, H.; Ballal, T.; Muqaibel, A.H.; Zhang, X.; Ai-Naffouri, T.Y. Air writing via receiver array-based ultrasonic source localization. *IEEE Trans. Instrum. Meas.* **2020**, *69*, 8088–8101. [CrossRef]

24. Guo, R.; He, Z.; Wang, W. Review of passive acoustic localization technique and impact point location methods. *Elem. Electroacoust.* **2010**, *34*, 48–51. [CrossRef]
25. Sun, S.; Xv, J.; Wang, W. Shock Wave Measurement and Time Difference of Arrival Analysis for Impact Point Positioning. *IEEE Trans. Instrum. Meas.* **2021**, *71*, 9600113. [CrossRef]
26. Bestagini, P.; Compagnoni, M.; Antonacci, F.; Sarti, A.; Tubaro, S. TDOA-based acoustic source localization in the space–range reference frame. *Multidimens. Syst. Signal Process* **2014**, *25*, 337–359. [CrossRef]
27. Dong, J.; Gao, L. Mathematical model of bullet shooting in any direction based on sensors distributed stereoscopically. In *2014 IEEE International Conference on Progress in Informatics and Computing*; IEEE: New York, NY, USA, 2014; Volume 2014, pp. 260–264. [CrossRef]
28. Bakhoum, E.G.; Cheng, M.H.M. Advanced Optical Microphone. *IEEE Sens. J.* **2013**, *14*, 7–14. [CrossRef]
29. Wang, Z.; Wen, G.; Wu, Z. Fiber optic method for obtaining the peak reflected pressure of shock waves. *Opt. Express* **2018**, *26*, 15199–15210. [CrossRef]
30. Fischer, B. Optical microphone hears ultrasound. *Nat. Photonics* **2016**, *10*, 356–358. [CrossRef]
31. Kim, D.; Hall, N.A. Towards a sub 15-dBA optical micromachined microphone. *J. Acoust. Soc. Am.* **2014**, *135*, 2664–2673. [CrossRef]
32. Milleri, N.; Valli, L.; Fueldner, M.; Wiesbauer, A.; Baschirotto, A. A 22-dBA Digital Optical MEMS Microphone. *IEEE J. Solid-State Circuits* **2024**, *59*, 2005–2018. [CrossRef]
33. Hu, X.; Yue, Y.; Cai, C.; Qi, Z. Temperature-robust optical microphone with a compact grating interferometric module. *Appl. Opt.* **2023**, *62*, 6072–6080. [CrossRef] [PubMed]
34. Xu, K.; Zong, Z.; Liu, D.; Wang, R.; Yu, L. Deep Learning-Based Sound Source Localization: A Review. *Appl. Sci.* **2025**, *15*, 7419. [CrossRef]
35. Jeong, I.; Huh, H.; Park, B.; Lee, A.; Jung, I.; Lee, S. MicGraphNet: Microphone graph network for cross-correlation-based time delay estimation for accurate sound source localization. *Measurement* **2026**, *258*, 119552. [CrossRef]
36. An, I.; An, G.; Kim, T.; Yoon, S.-E. Microphone Pair Training for Robust Sound Source Localization with Diverse Array Configurations. *IEEE Robot. Autom. Lett.* **2024**, *9*, 319–326. [CrossRef]
37. Fu, W.; Zhou, R.; Gao, Y.; Guo, Z.; Yu, Q. Damage Source Localization in Concrete Slabs Based on Acoustic Emission and Machine Learning. *IEEE Sens. J.* **2025**, *25*, 11622–11635. [CrossRef]
38. Cai, R.; Ni, J.; Tian, H. Design and improvement of a light-interference-resistant light curtain target. *Opt. Tech.* **2006**, *5*, 790–7922. [CrossRef]
39. Pouretedal, H.; Sattar, S.; Zare, A. Improved luminosity of a new tracer pyrotechnic of Mg:BaO_2:$Ba(NO_3)_2$:Viton using response surface methodology. *J. Therm. Anal. Calorim.* **2023**, *148*, 5209–5216. [CrossRef]
40. Lo, K.W. A matched-field processing approach to ranging surface vessels using a single hydrophone and measured replica fields. *J. Acoust. Soc. Am.* **2021**, *49*, 1466. [CrossRef]
41. Duan, C.; Ni, J.; Tian, H.; He, B.; Li, J. The effect of muzzle blast wave on light screen in external ballistic measurement. *Front. Phys.* **2025**, *13*, 1517445. [CrossRef]
42. Noack, J.; Hammer, D.X.; Noojin, G.D.; Rockwell, B.A.; Vogel, A. Influence of pulse duration on mechanical effects after laser-induced breakdown in water. *J. Appl. Phys.* **1998**, *83*, 7488–7495. [CrossRef]
43. Mur, J.; Reuter, F.; Kočica, J.J.; Lokar, Ž.; Petelin, J.; Agrež, V.; Ohl, C.D.; Petkovšek, R. Multi-frame multi-exposure shock wave imaging and pressure measurements. *Opt. Express* **2022**, *30*, 37664–37674. [CrossRef]
44. Li, H.; Zhang, X.; Zhang, X.; Gao, J. Warhead Fragments' Distribution Measurement Method by a Multiscreen Sensors' Intersection Test Mechanism and Equivalent Target Damage Probability Calculation. *IEEE Trans. Instrum. Meas.* **2021**, *70*, 7004109. [CrossRef]